Journal of Physics: Conference Series **3230** (2026) 012002 doi:10.1088/1742-6596/3230/1/012002

Modal triadic interaction informed restricted nonlinear models

Alexandra C. Risha[1], Emma Lenz[2], Bianca Viggiano[3], H. Jane Bae[2], and Dennice F. Gayme[1]

[1] Department of Mechanical Engineering, Johns Hopkins University, Baltimore, MD 21218 USA
[2] Graduate Aerospace Laboratories, California Institute of Technology, Pasadena, CA 91125 USA
[3] Génie Mécanique, Polytechnique Montréal, Montreal, Quebec H3T 1J4 Canada

E-mail: arisha1@jh.edu

Abstract. Turbulent flows involve high-dimensional nonlinear interactions across a range of spatial and temporal scales, and the need to capture such interactions makes them challenging to model and simulate. We present a resolvent-based framework to guide scale selection in reduced-order models of turbulence. Resolvent analysis offers a physics-based framework to decompose the Navier-Stokes equation into linear and nonlinear components and to identify the most amplified flow structures. Building on this framework, we introduce an energy exchange coefficient that directly quantifies nonlinear energy transfer between resolvent modes, enabling an energy-based ordering of triadic interactions in turbulent channel flow without relying on data-driven closures. Triads with large interaction coefficients are incorporated into the augmented restricted nonlinear (ARNL) model, which is a physics-based reduced-order representation that requires specification of streamwise flow scales permitted to interact nonlinearly (large-scales) and small-scale streamwise perturbations whose linear evolution is a function of these large scales. Resolvent-informed ARNL simulations are shown to produce normal Reynolds stresses, energy spectra, and energy transport consistent with DNS data. These results demonstrate the potential of the resolvent-based approach for identifying important nonlinear interactions and as a tool for improving physics-grounded turbulence modeling.

1 Introduction

Turbulence is characterized by interactions across a wide range of spatial and temporal scales. Linear mechanisms such as modal amplification and instability play an important role in shaping flow structures, but it is the nonlinear interactions that redistribute energy across scales and sustain turbulence [1–4]. These nonlinear processes are high-dimensional and computationally expensive to resolve; however, they are central to capturing the multiscale dynamics of turbulence [3]. Reduced order models can reduce the computational burden, but obtaining accurate representations and their utility for prediction or control requires that they retain essential aspects of the physics. Therefore, developing a better understanding of the key nonlinear processes in turbulence is critical both for uncovering fundamental aspects of the dynamics and informing tractable tools for analysis, prediction, and control.

Resolvent analysis is a powerful equation-based tool to understand the relationship between linear and nonlinear effects. In this framework, the Navier-Stokes equations (NSE) are decomposed into linear and nonlinear components, where the nonlinear terms are interpreted as a forcing term to the linear dynamics.

Journal of Physics: Conference Series **3230** (2026) 012002 doi:10.1088/1742-6596/3230/1/012002

The resulting input-output relationship is captured by the resolvent operator, which acts as a 'transfer function' (spatio-temporal frequency response operator) mapping the forcing to the system's response, see e.g. [5]. In resolvent analysis, a singular value decomposition (SVD) of the resolvent operator identifies the most amplified flow responses and the forcing structures that generate them, thereby revealing the coherent structures and amplification mechanisms that dominate the linearized turbulent dynamics, see e.g., [6–11]. Importantly, resolvent analysis requires only the mean flow profile and boundary conditions. It therefore does not rely on full-scale simulations or experimental data. This makes it a computationally efficient yet physics-grounded tool for dissecting the interplay between linear amplification mechanisms and nonlinear energy transfer in turbulence.

The interpretation of the nonlinear terms of the NSE an external forcing acting on the linear dynamics of the flow [6] isolates the linear amplification mechanisms without resolving the full nonlinear interactions. It is common to assume broadband forcing (i.e., delta correlated in space and time), where all modes are weighted equally and every forcing mode is excited with unit amplitude. Statistical modeling or data-driven techniques can also provide insight into the feedback between the output modes and the nonlinear forcing term. Stochastic forcing or colored noise can be used to empirically model the forcing term [12, 13]. Alternatively, extraction of flow field data from high fidelity simulations can also be done to inform weighting of the resolvent modes [14–16]. While these techniques provide information about important structures in the flow, they rely on empirical data and it may be difficult to extract structural features or other information about the most amplified modes beyond that obtained through analysis using white-noise forcing assumptions [11, 15].

The structure of the forcing terms has been further examined to determine the critical nonlinear interactions governing the flow. Resolvent analysis techniques have used modal decomposition to capture triadic relationships between modes across a wide range of flow configurations [15, 17–22]. Specifically, the nonlinear forcing can be approximated by computing the interaction between resolvent modes [15]. This approach accurately predicts mode amplitudes, correctly capturing the spatial structure of the most energetic mode in low-rank regions and reproducing mode shapes computed by data-driven methods [15]. High fidelity studies [18, 23, 24] also highlight the structured energy redistribution across scales by specific mode interactions, further motivating the incorporation of such dynamics into reduced-order modal frameworks.

Nonlinear energy transfer predicted by the first resolvent mode using true velocity flow field data was compared to the Fourier modes in DNS [18]. Results suggest the nonlinear transfer was minimal for the optimal resolvent mode, compared to production and dissipation, but had a major role in redistributing energy in the DNS. Suppressing the principal resolvent forcing mode, which has contributions from limited nonlinear interactions, was found to inhibit turbulence within a minimal flow unit [17]. Using simulation data, flow structures contributing to the principal nonlinear forcing were identified, which facilitate key nonlinear interactions in the self-sustaining process of near-wall turbulence. [20] also showed the importance of large-scale structures interacting with small-scale gradients extracted from simulation data to model the nonlinear forcing. These studies rely on simulation flow field data to model the nonlinearity, offering valuable insight into the forcing structure and modal interactions; however, they lack a computationally efficient method for determining these relationships.

In this work, we extend the resolvent analysis framework to directly compute nonlinear interactions between response and forcing modes. While standard resolvent analysis computes the linear effect of forcing modes onto response modes, we "close the loop" by computing the nonlinear contribution of response modes back into the forcing term. Specifically, we use a nonlinear energy exchange coefficient, defined by computing the nonlinear term of the NSE in terms of the response modes and projecting it onto the forcing modes. This formulation provides a self-contained framework that relies solely on the outputs of resolvent analysis and a turbulent mean profile, thereby offering a physics-based alternative to data-driven approaches.

We test the effectiveness of this approach by applying it to parametrize an augmented restricted nonlinear (ARNL) model [25] which requires specification of its streamwise wave number support. The ARNL representation is an extension of the restricted nonlinear (RNL) model, which restricts streamwise varying flow structures contributing to the dynamics, see e.g., [26–28]. Based on the prevalence and dynamical importance of streamwise coherent structures in wall-bounded turbulence [29–31], the RNL model is obtained by first decomposing the total flow field into a streamwise averaged mean flow (large-scale) and perturbations about that mean (small-scales). The nonlinear interactions are neglected which do not contribute to the dynamics of the streamwise averaged mean (large-scale) modes. RNL representations have been shown to produce self-sustaining turbulence in canonical wall-bounded flows at low to moderate Reynolds numbers with the perturbation dynamics supported by a single streamwise varying mode (i.e., non-zero wave number when the flow is represented using Fourier basis functions) [26, 27, 32, 33].

The accuracy of the statistics, spectra, and energy transport of the RNL turbulence is improved when the permitted wavelengths of the corresponding structures fall within the peak range of the outer-layer pseudo-dissipation spectra [28]. However, the accuracy breaks down for high-Reynolds numbers when scale separation becomes increasingly important. Limiting nonlinear interactions between streamwise scales to those involving or contributing to the streamwise constant mean becomes too restrictive to capture the energy transfer across scales that becomes increasingly important as Reynolds numbers increase [25].

The ARNL model sought to overcome the limitation of the RNL model at large Reynolds numbers by permitting additional streamwise varying structures to interact nonlinearly. A similar approach has been taken in generalized quasilinear (GQL) models where a spectral cutoff in both the streamwise and spanwise domains defines the spanwise and streamwise scales permitted to act nonlinearly (i.e. the large-scales), see e.g. [34–36]. RNL models differ in that they use a band-pass filter to determine the streamwise modes supporting the perturbation dynamics, rather than based on the spectral cutoff. The ARNL framework similarly imposes the streamwise scales permitted to interact nonlinearly as part of the large-scale dynamics. The small scales are then restricted to the region surrounding the peak of the outer-layer pseudo dissipation spectra in pairs that maintain triadic consistency with the nonlinear interactions within the mean dynamics [25]. This ARNL framework has been shown to provide improved performance over RNL models at moderate Reynolds numbers $Re_\tau > 550$ [25] when the additional large scale was chosen to coincide with the half-channel height. Applications to study flow over riblets also illustrated the improved ability of the ARNL framework in capturing physics associated with drag alteration in these flows [37]. A benefit of this framework is the ability to impose hierarchical coupling of modes (i.e., via triadic relationships) that enables increasing model fidelity with limited increases in computational cost.

While the previous work highlighted the promise of the ARNL framework, the selection of the large-scale and the triadically consistent small scales was ad hoc [25]. Furthermore, the selection of the half-channel height makes physical sense as a large-scale; it is still unclear how to systematically select additional scales. As discussed above, resolvent analysis based methods have proven effective in identifying energetically important nonlinear interactions. These results motivate the use of the resolvent analysis approach described above to select the streamwise wavenumber support of the ARNL model.

We investigate the resolvent analysis informed ARNL dynamics in a channel at $Re_\tau = 180$. While this Reynolds number is lower than those where scale separation becomes dominant, this well-studied case offers advantages in terms of computational tractability and availability of both DNS and RNL data for comparison. As the RNL model has already been shown to produce good agreement with DNS at this Reynolds number, it also allows us to isolate the changes arising from the additional nonlinear interactions permitted in the RNL framework. We first demonstrate that using the resolvent forcing modes to obtain the nonlinear interaction coefficients yields results consistent with previous data-driven methods. We then focus on streamwise wave numbers and select triads that have high nonlinear interaction coefficients as candidate parametrizations for the ARNL models and select cases based on the extent to which the small scales fall within the optimal range identified in previous DNS studies. The resulting resolvent-informed ARNL simulations are shown to improve upon RNL predictions of normal Reynolds stresses, energy spectra, and energy transport.

The remainder of this paper is organized as follows. Section 2 introduces the methodology and governing equations for both the resolvent analysis and the ARNL model. Section 3 describes the numerical configuration and solver details. Section 4 presents simulation results and associated discussion. Finally, the paper summarizes key findings and outlines future work in section 5.

2 Methods

We consider turbulent channel flow at friction Reynolds number $Re_\tau = 180$, defined by the friction velocity u_τ, the kinematic viscosity ν, and the channel half height δ. The streamwise, wall-normal, and spanwise directions are denoted as x_1, x_2, and x_3, respectively. The velocity and pressure fields are respectively denoted as $\boldsymbol{u_T}$ and p_T. In the following subsections, we describe two reduced-order representations, resolvent analysis and the augmented restricted nonlinear model (ARNL).

In resolvent analysis, the velocity and pressure fields are decomposed as $\boldsymbol{u_T} = \boldsymbol{U} + \boldsymbol{u}$ and $p_T = P + p$ respectively. The mean velocity is assumed to be a one-dimensional streamwise velocity profile, $\boldsymbol{U} = (U_1(x_2), 0, 0)$, defined as the time and horizontally averaged (x_1 and x_3) turbulent mean velocity profile. The corresponding fluctuating velocity field is denoted $\boldsymbol{u}(x_1, x_2, x_3, t) = (u_1, u_2, u_3)$. A similar decomposition is applied to the pressure field, where $P(x_2)$ and $p(x_1, x_2, x_3, t)$ are the respective mean and fluctuating components.

In the ARNL model, the velocity and pressure fields are decomposed into a large-scale mean flow and perturbations about that mean as $\boldsymbol{u_T} = \boldsymbol{\mathcal{U}} + \widetilde{\boldsymbol{u}}$ and $p_T = \mathcal{P} + \widetilde{p}$. The large-scale mean velocity field is defined as $\boldsymbol{U}(x_1, x_2, x_3, t) = \langle \boldsymbol{u_T} \rangle_l$ and small-scale perturbations are denoted $\widetilde{\boldsymbol{u}}(x_1, x_2, x_3, t)$. The $\langle \cdot \rangle_l$ denotes a filtering operation that restricts the streamwise wavenumber support to a predefined set of large-scales $\mathcal{L}$. Further details of the streamwise wavenumber support comprising the large- and small-scales are provided in §2.2. An analogous filtering is employed to define the mean and perturbation components of the pressure field.

2.1 Resolvent Analysis

To form the resolvent operator, the non-dimensional incompressible NSE are first linearized about the mean flow $\boldsymbol{U}$ and Fourier transformed in the homogeneous directions (x_1, x_3) and time, resulting in the linear system

$$\begin{bmatrix} \widehat{\boldsymbol{u}}(x_2; k_1, k_3, \omega) \\ \widehat{p}(x_2; k_1, k_3, \omega) \end{bmatrix} = \mathcal{H}(k_1, k_3, \omega) \begin{bmatrix} \widehat{\boldsymbol{f}}(x_2; k_1, k_3, \omega) \\ 0 \end{bmatrix}, \tag{1}$$

with resolvent operator

$$\mathcal{H}(k_1, k_3, \omega) = \begin{bmatrix} -\mathrm{i}(\omega - k_1 U_1) - \nabla^2/Re_\tau & \partial U_1/\partial x_2 & 0 & \mathrm{i}k_1 \\ 0 & -\mathrm{i}(\omega - k_1 U_1) - \nabla^2/Re_\tau & 0 & \partial/\partial x_2 \\ 0 & 0 & -\mathrm{i}(\omega - k_1 U_1) - \nabla^2/Re_\tau & \mathrm{i}k_3 \\ -\mathrm{i}k_1 & -\partial/\partial x_2 & -\mathrm{i}k_3 & 0 \end{bmatrix}^{-1}, \tag{2}$$

where $\nabla^2 = -(k_1^2 + k_3^2) + \partial^2/(\partial x_2)^2$, and ω is the temporal frequency. k_1 and k_3 are the wavenumbers in the respective streamwise and spanwise directions, defined as $k_i = 2\mathrm{n}\pi\delta/L_i$, where n is the wave index integer and L_i is the domain length in the x_i direction. The vector $[\widehat{\boldsymbol{u}},\ \widehat{p}]^\top = [\widehat{u}_1,\ \widehat{u}_2,\ \widehat{u}_3,\ \widehat{p}]^\top$ comprises the states, $[\widehat{\boldsymbol{f}},\ 0]^\top = \left[\widehat{f}_1,\ \widehat{f}_2,\ \widehat{f}_3, 0\right]^\top$ is the nonlinear forcing vector consisting of the nonlinear terms, $\widehat{(\cdot)}$ indicates quantities that have been Fourier transformed (in x_1, x_3 and t), and superscript $\top$ indicates the transpose of a matrix. In what follows, we omit the x_2 in the argument of transformed quantities for brevity.

We perform a singular value decomposition (SVD) on the resolvent operator $\mathcal{H}$ in (2) by applying a Schmidt decomposition following [6] such that

$$\begin{bmatrix} \widehat{\boldsymbol{u}}(k_1, k_3, \omega) \\ \widehat{p}(k_1, k_3, \omega) \end{bmatrix} = \sum_{n=1}^{4N_2} \sigma_n(k_1, k_3, \omega) \left\langle \widehat{\boldsymbol{f}}(k_1, k_3, \omega)\ ,\ \widehat{\boldsymbol{\phi}}_n(k_1, k_3, \omega) \right\rangle \begin{bmatrix} \widehat{\boldsymbol{\psi}}_n(k_1, k_3, \omega) \\ \widehat{\psi}_{n,p}(k_1, k_3, \omega) \end{bmatrix}, \tag{3}$$

where

$$\langle \boldsymbol{a}(x_2), \boldsymbol{b}(x_2) \rangle = \int_0^{2\delta} \boldsymbol{b}^*(x_2)\ \boldsymbol{a}(x_2)\, \mathrm{d}x_2 \tag{4}$$

is the inner product corresponding to the kinetic energy norm. The singular values σ_n are the gains ordered such that $\sigma_1 \geq \sigma_2 \geq \cdots \geq 0$, the right singular vectors $\widehat{\boldsymbol{\Phi}}_n = [\widehat{\boldsymbol{\phi}}_n, 0]^\top = [\widehat{\phi}_{n,1}, \widehat{\phi}_{n,2}, \widehat{\phi}_{n,3}, 0]^\top$ are the resolvent forcing modes, and the left singular vectors $\widehat{\boldsymbol{\Psi}}_n(k_1, k_3, \omega) = [\widehat{\boldsymbol{\psi}}_n, \widehat{\psi}_{n,p}]^\top = [\widehat{\psi}_{n,1}, \widehat{\psi}_{n,2}, \widehat{\psi}_{n,3}, \widehat{\psi}_{n,p}]^\top$ are the resolvent response modes. N_2 is the number of grid points in the wall-normal direction, and $4N_2$ is the number of modes associated with each (k_1, k_3, ω) input. The superscript $*$ indicates the complex conjugate.

The nonlinear forcing term can be written in terms of a convolution of the velocity vector

$$\widehat{\boldsymbol{f}}(k_1, k_3, \omega) = \sum_{\substack{k_1', k_3', \omega' \\ (k_1, k_3) \neq (0,0)}} (\widehat{\boldsymbol{u}}(k_1', k_3', \omega') \cdot \nabla)\, \widehat{\boldsymbol{u}}(k_1 - k_1', k_3 - k_3', \omega - \omega'), \tag{5}$$

where $\nabla = [ik_1, \partial/\partial x_2, ik_3]^\top$. Since resolvent analysis only considers amplification of fluctuations with respect to the mean profile, the associated $(k_1, k_3) = (0, 0)$ mode is omitted. For brevity, we abbreviate a quantity $q(k_1, k_3, \omega)$ as q, $q(k_1', k_3', \omega')$ as q', and $q(k_1'', k_3'', \omega'')$ as q'' where $k_1'' = k_1 - k_1'$, $k_3'' = k_3 - k_3'$, and $\omega'' = \omega - \omega'$. Expressing the velocity vector as a linear sum of resolvent response modes weighted by the nonlinear forcing mode weight [38],

$$\chi_n(k_1, k_3, \omega) = \left\langle \widehat{\boldsymbol{f}}(k_1, k_3, \omega)\ ,\ \widehat{\boldsymbol{\phi}}_n(k_1, k_3, \omega) \right\rangle. \tag{6}$$

Then using the expression for $\widehat{\boldsymbol{u}}$ given in equation (3), we can recast the nonlinear term in equation (5) as

$$\widehat{\boldsymbol{f}} = \sum_{l,m=1}^{4N_2} \sum_{\substack{k_1',k_3',\omega' \\ (k_1,k_3)\neq(0,0)}} \left(\sigma_l' \chi_l' \widehat{\boldsymbol{\psi}}_l' \cdot \nabla\right) \left(\sigma_m'' \chi_m'' \widehat{\boldsymbol{\psi}}_m''\right). \tag{7}$$

We can determine the contribution of the nonlinear interaction of the response modes to the forcing modes by projecting $\widehat{\boldsymbol{f}}$ onto the forcing modes and rearranging such that

$$\left\langle \widehat{\boldsymbol{f}},\ \widehat{\boldsymbol{\Phi}}_n \right\rangle = \left\langle \sum_{l,m=1}^{4N_2} \sum_{\substack{k_1',k_3',\omega' \\ (k_1,k_3)\neq(0,0)}} \sigma_l' \sigma_m'' \chi_l' \chi_m'' \left(\widehat{\boldsymbol{\psi}}_l' \cdot \nabla\right) \widehat{\boldsymbol{\psi}}_m'',\ \widehat{\boldsymbol{\Phi}}_n \right\rangle, \tag{8}$$

which provides a relationship between the weights of a triad, comprising a forcing mode and two response modes. To calculate the full nonlinear forcing in equations (7) and (8), additional flow field information (e.g, DNS data or other empirical data) is needed to compute the mode weights χ_l' and χ_m''. Instead, we define a nonlinear interaction coefficient

$$\alpha_n(k_1, k_3, \omega; k_1', k_3', \omega', l, m) = \sigma_l' \sigma_m'' \left\langle \left(\widehat{\boldsymbol{\psi}}_l' \cdot \nabla\right) \widehat{\boldsymbol{\psi}}_m'' \ ,\ \widehat{\boldsymbol{\Phi}}_n \right\rangle, \tag{9}$$

which only depends on information provided via resolvent analysis. Strictly speaking, α_n reflects the strength of a nonlinear interaction based on the structure and geometry of the forcing and response modes forming the triad and the amplification (σ) of the resolvent operator. Some triads may have structures and linear amplifications that favor nonlinear energy exchange, and therefore have large values of α_n, regardless of the total amount of energy exchanged. If the nonlinear forcing is assumed to be broadband ($\chi = 1$ for all modes), then α_n also reflects the full nonlinear energy exchange; under this assumption, the triad with the largest α_n coefficient would also have the largest nonlinear contribution. Since nonlinear forcing is not broadband generally, we define α_n to be a coefficient that does not depend on the mode weights χ_l' and χ_m''. This approach enables us to analyze the α_n coefficients to identify interactions that have large nonlinear contribution without the need for data-driven methods. Triads with large α_n coefficients will be used to parameterize the ARNL model described in the next section.

2.2 Augmented Restricted Nonlinear Model

The ARNL model governing equations are formed from the NSE by first neglecting nonlinear interactions between streamwise wavenumbers that do not contribute to the large scales $k_1 \in \mathcal{L}$ and then defining the set $\mathcal{S}$ of small scales supporting the perturbation dynamics [25,37]. The resulting evolution equations for the ARNL mean and perturbation dynamics are respectively given by

$$\partial_t \boldsymbol{\mathcal{U}} + \langle \boldsymbol{\mathcal{U}} \cdot \nabla \boldsymbol{\mathcal{U}} \rangle_l + \nabla \mathcal{P} - \nabla^2 \boldsymbol{\mathcal{U}}/Re_\tau = -\langle \widetilde{\boldsymbol{u}} \cdot \nabla \widetilde{\boldsymbol{u}} \rangle_l\,, \tag{10}$$

$$\partial_t \widetilde{\boldsymbol{u}} + \langle \boldsymbol{\mathcal{U}} \cdot \nabla \widetilde{\boldsymbol{u}} \rangle_s + \langle \widetilde{\boldsymbol{u}} \cdot \nabla \boldsymbol{\mathcal{U}} \rangle_s + \nabla \widetilde{p} - \nabla^2 \widetilde{\boldsymbol{u}}/Re_\tau = 0. \tag{11}$$

Here $\langle\cdot\rangle_l$ indicates filtering that restricts the output of the operation to the large-scales, i.e., $k_1 \in \mathcal{L}$ and $\langle\cdot\rangle_s$ denotes analogous filtering limiting to the small-scales $k_1 \in \mathcal{S}$. The dynamics in equation (10) comprise only large-scales ($k_1 \in \mathcal{L}$) and those equation (11) include only small-scales ($k_1 \in \mathcal{S}$). The streamwise wave number support of the ARNL large-scale dynamics $\mathcal{L}$ includes non-zero streamwise modes ($k_1 \neq 0$) in addition to the streamwise average mean ($k_1 = 0$) comprising the RNL large scale, see e.g. [28,39]. To emphasize that these modes represent the ARNL large scales, we will denote them using a capital K_1' in the remainder of the paper, where the $'$ is used for consistency with the notation used in §2.1. Consistent with the definitions in the resolvent framework, the nonlinear interactions between streamwise scales contributing to the large-scale dynamics are constrained to satisfy $K_1' + k_1'' = k_1$. The full range of nonlinear interactions between spanwise scales also satisfies $K_3' + k_3'' = k_3$. The set $\mathcal{S}$ contains the small-scale non-zero modes (i.e., $k_1, k_1'' \neq 0$) which support the perturbation dynamics.

As the ARNL framework builds on the RNL modeling paradigm, the large scales always include the streamwise constant mean, i.e., the $K_1' = 0$ mode. The non-zero streamwise scales contributing to the ARNL dynamics will be determined based on resolvent analysis and previous analysis demonstrating the accuracy of the RNL model when $k_1'', k_1 \in \mathcal{S}$ are restricted to those corresponding to the peak region of the outer-layer surrogate dissipation spectrum [28].

3 Numerical Configuration

In this section, we describe the numerical implementation of the ARNL model and resolvent analysis. We also introduce the configuration of the DNS used to obtain the mean profile required by resolvent analysis and to validate the ARNL results. As the resolvent computations rely on the DNS mean profile, we present the DNS/ARNL configuration first.

3.1 Direct Numerical and Augmented Restricted Nonlinear Model Simulations

DNS and ARNL simulations employ a modified version of the open-source code LESGO (lesgo.jhu.edu). The code is pseudo-spectral, employing Fourier transforms in the streamwise and spanwise directions. The wall-normal direction uses second-order central finite differencing. Time advancements employ the Crank-Nicholson scheme for wall-normal diffusive terms and Adams-Bashforth for the remaining terms [25, 37]. Periodic boundary conditions are applied in the streamwise and spanwise directions. No-slip and no-penetration boundary conditions are applied at both the top and bottom walls.

The streamwise, wall-normal, and spanwise domain sizes for the DNS are $[L_1, L_2, L_3] = [\pi, 2, \pi/2]\delta$. The grid resolution is $[N_1, N_2, N_3] = [64, 128, 64]$ resulting in $\Delta x_1^+ = 8.84$, $\max(\Delta x_2^+) = 7.39$, and $\Delta x_3^+ = 4.42$, where the superscript '+' denotes normalization in viscous units. A hyperbolic tangent stretching function [40] is applied in the wall-normal direction to ensure 15 grid points lie within $0 < x_2^+ < 5$. A maximum stretching ratio of 1.08 is maintained. ARNL simulations use the same x_2–x_3 (cross-plane) resolution and domain extents as the DNS. There is no physical space streamwise grid in the ARNL simulations, i.e., due to the restriction in the streamwise wave number support of the dynamics, the nonlinearity is computed in the Fourier domain for computational efficiency (see details in [25, 37]). However, for consistency with the DNS and resolvent analysis computations, the DNS streamwise domain length L_1 is used to define wavenumbers [25].

We performed DNS for a standard channel where $[L_1, L_2, L_3] = [2\pi, 2, \pi]\delta$ and compared to another larger channel where $[L_1, L_2, L_3] = [4\pi, 2, \frac{4\pi}{3}]\delta$ [41] to ensure the small channel (used above) maintained similar dynamics. A comparison of the mean streamwise velocity and cross-plane Reynolds shear stress for the different domain sizes showed minimal differences. Therefore, the small domain was used in the results presented below to maintain computational efficiency in the ARNL simulations and the resolvent analysis computations.

3.2 Resolvent Mode Computations

The resolvent modes are computed using the horizontally and time-averaged mean streamwise velocity profile from the DNS data. The streamwise and spanwise wavelengths are chosen to match the discretized wavelengths in the DNS and ARNL simulations. Wall-normal points are located at the same locations as the DNS and ARNL grid points with $N_2 = 128$. Wall-normal differentiation uses a second-order central finite difference scheme with the same nonuniform grid for consistency with the DNS and ARNL implementation described above. The integration in the inner product calculation accounts for wall-normal grid stretching.

The interactions responsible for the largest nonlinear energy transfer are evaluated by calculating α_n across all streamwise and spanwise triad combinations. Since structures with zero temporal frequency are known to contribute significantly to the streamwise constant (i.e, $k_1 = 0$) dynamics, we only consider modes that are constant in time where ω, ω', and $\omega'' = 0$ [17, 20]. Similarly, only the top 4 most amplified forcing and response pairs are considered for each wavenumber input. Only positive wavenumbers are reported for brevity.

4 Results and Discussion

This section first describes the streamwise and spanwise scales (k_1, k_3) and the nonlinear scale interactions $k_1 = K_1'$[1] $+ k_1''$ and $k_3 = K_3' + k_3''$ associated with the largest nonlinear energy coefficients α in (9). We then select the triads $k_1 = K_1' + k_1''$ associated with large values of α and small scales consistent with the RNL modeling paradigm to parametrize the ARNL simulations. Finally, the turbulent statistics of the resolvent-informed ARNL simulations are compared to a full-channel DNS [41] and a half-channel RNL simulation [28].

Figure 1(a) presents the normalized nonlinear energy transfer coefficient α/α_{max} computed from (8) and (9) for a range of (k_1, k_3) wave number pairs where the size and color of the marker are used to indicate the relative magnitude for different pairs. This α/α_{max} is obtained by computing all possible

[1]Recall: We have replaced k_1' in equation (5) k_1'' with K_1' here to explicitly indicate that these wavenumbers are in the set $\mathcal{L}$ for the ARNL decomposition.

interactions (k' and k'' combinations), ranking them by magnitude, and reporting the largest value for a given (k_1, k_3) pair. The results in Figure 1(a) suggest the largest energy transfer occurs for a forcing mode $\widehat{\boldsymbol{\phi}}_n(0, 8, \omega = 0)$, i.e., with wavenumbers $(k_1, k_3) = (0, 8)$. The triad components associated with $\widehat{\boldsymbol{\phi}}_n(0, 8, \omega = 0)$ arise from the response mode $(\widehat{\boldsymbol{\psi}}_n)$ wavenumber pairs $(K_1', K_3') = (0, 4)$ and $(k_1'', k_3'') = (0, 4)$. These results indicate structures that are very long in the streamwise direction with spanwise wavenumbers 4 or 8 allow for the largest nonlinear energy transfer.

Our results align with previous studies which aim to identify important modes related to nonlinear energy exchange. The Fourier mode $(k_1, k_3) = (0, 8)$ was previously identified as having the largest turbulent kinetic energy and nonlinear energy transfer in a DNS study of a minimal channel at $Re_\tau = 180$ [18]. This aligns with our findings (in figure 1(a)), though in contrast to [18], our method does not use DNS data, but instead only depends on quantities stemming from the resolvent operator. Further, in figure 1(a), we observe the (k_1, k_3) pairs that are constant in the streamwise direction (i.e., $k_1 = 0$) have the largest nonlinear energy coefficients. Prior studies also indicate $k_1 = 0$ as important to the flow dynamics [17–20, 24], again, confirming that our method captures similar trends without using DNS or external data. This finding that the most dominant mode pairs contain $k_1 = 0$ provides further support for the development of reduced-order models that emphasize streamwise coherent dynamics. One such model is the ARNL model where nonlinear interactions with the streamwise mean are being directly computed.

The ARNL framework requires specification of the non-zero streamwise modes to be retained in both the large and small scale dynamics. To isolate nonlinear interactions contributing to the associated energy transfer, we exclude triads involving a streamwise average component, i.e., we do not include computations for $k_1 = K_1' = k_1'' = 0$. We then compute α/α_{max} for all possible streamwise triads that do not include a zero mode (i.e., for all triads such that $k_1, K_1', k_1'' \neq 0$). As the ARNL model maintains full nonlinearity in the spanwise direction, all spanwise triads are simulated [25, 28], so we only investigate the relative ordering of streamwise triads. Figure 1(b) shows α/α_{max} for the K_1' and k_1'' values that provide the largest response for each k_1 over all of the mode combinations, where again the relative strength is indicated by the darker color and larger markers. Figure 1(c) provides a magnified view of the combinations associated with the largest values of α/α_{max}. Here, the streamwise-varying triadic interaction with the largest α/α_{max} is $(K_1', k_1'', k_1) = (2, 2, 4)$, followed by $(K_1', k_1'', k_1) = (2, 4, 6)$ and $(K_1', k_1'', k_1) = (2, 6, 8)$. Similar trends can be seen in [20], where an interaction coefficient similar to that in (8) was defined to investigate the relative importance of interactions involving streamwise large-scale structures using a projection onto DNS data rather than resolvent forcing modes.

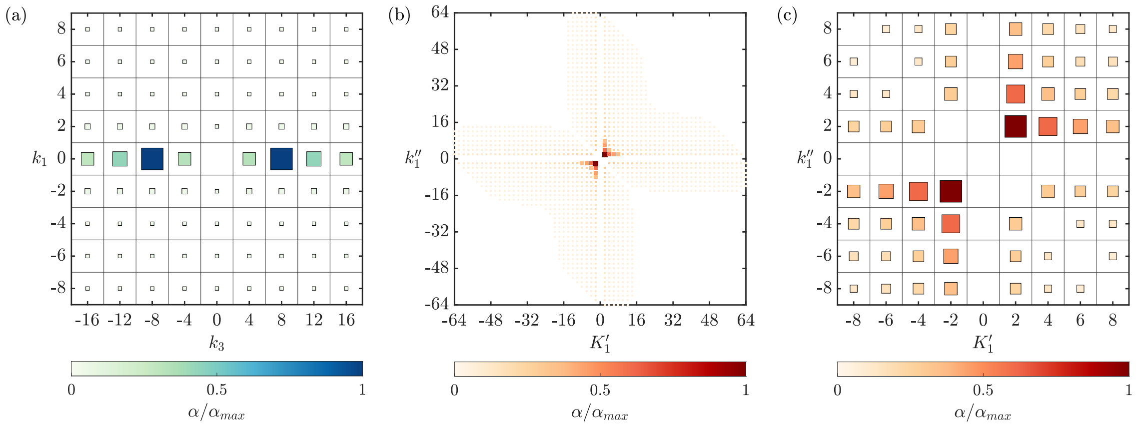

Figure 1: Normalized nonlinear energy transfer coefficient, α/α_{max}, for wave number combinations. (a) Spanwise and streamwise wavenumber pairs (partial domain shown), (b) streamwise triadic interaction with mean components filtered (full domain shown), and (c) magnified view of panel (b). Color and marker size denote interaction magnitude, where darker shades and larger squares correspond to stronger interactions. Empty boxes indicate streamwise mean mode filtering. The horizontal axis in panels (b) and (c) is defined as $K_1' = k_1'$.

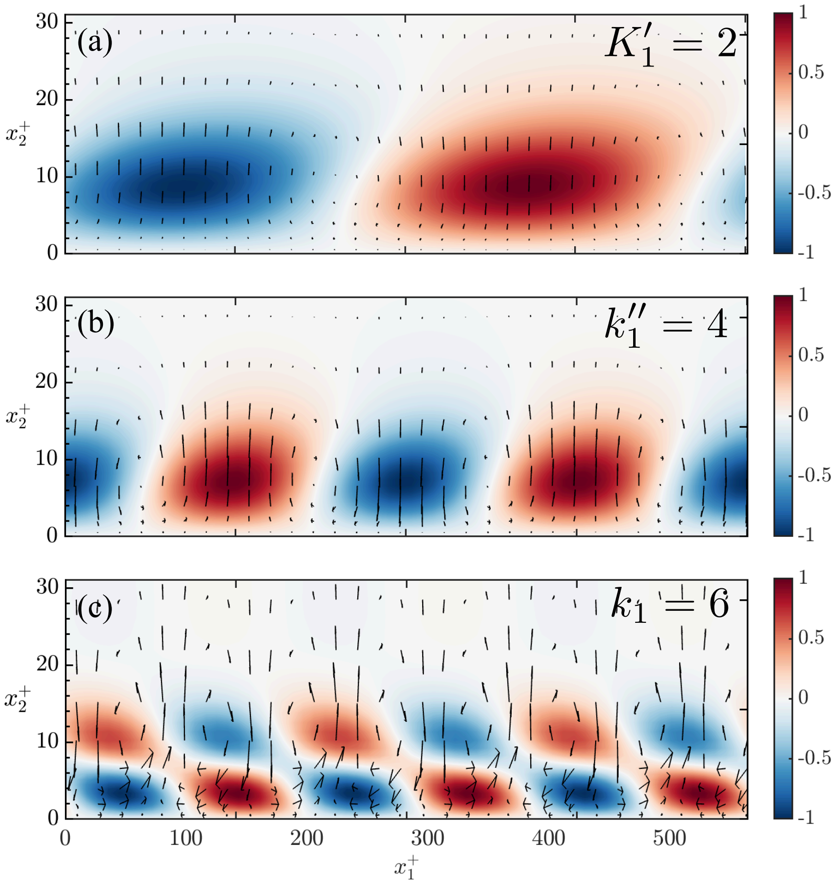

Figure 2: Visualization of resolvent modes associated with the triad $(K_1', k_1'', k_1) = (2, 4, 6)$, with color indicating streamwise components and arrows indicating cross-flow components. (a) Response mode $K_1' = 2$ and (b) response mode $k_1'' = 4$, inverse Fourier-transformed to show spatial structures, with colorbar indicating the normalized streamwise component $\widehat{\psi}_1/|\widehat{\psi}_{1,max}|$ and arrows indicating the wall-normal and spanwise components $\widehat{\psi}_2/|\widehat{\psi}_{1,max}|$ and $\widehat{\psi}_3/|\widehat{\psi}_{1,max}|$. (c) Forcing mode $k_1 = 6$, inverse Fourier-transformed to show spatial structures, with colorbar indicating the normalized streamwise component $\widehat{\phi}_1/|\widehat{\phi}_{1,max}|$ and arrows indicating the wall-normal and spanwise components $\widehat{\phi}_2/|\widehat{\phi}_{1,max}|$ and $\widehat{\phi}_3/|\widehat{\phi}_{1,max}|$. Wall-normal direction is cropped for visualization.

In what follows, we focus on the $(K_1', k_1'', k_1) = (2, 4, 6)$ and $(K_1', k_1'', k_1) = (2, 6, 8)$ triads because the small scales $k_1 = 2$ and $k_1'' = 4$ associated with the $(K_1', k_1'', k_1) = (2, 2, 4)$ mode, correspond to streamwise wavelengths outside of the peak region of the outer layer pseudo dissipation spectra. Prior work with the RNL model suggests that limiting the small-scale structures to this region produces optimal statistics within the RNL framework [28, 33]. This choice has also been shown to produce good results in prior ARNL studies [25, 37] and will be further analyzed herein.

Figure 2 visualizes the resolvent modes associated with the triadic relationship $(K_1', k_1'', k_1) = (2, 4, 6)$ in the x_1-x_2 plane. This combination produces the largest α/α_{max} excluding zero-wavenumber modes and repeating triad entries. Specifically, figure 2(a) shows response mode $\widehat{\boldsymbol{\psi}}_{l=1}(K_1' = 2, K_3' = -28, \omega' = 0)$, figure 2(b) shows response mode $\widehat{\boldsymbol{\psi}}_{m=1}(k_1'' = 4, k_3'' = 44, \omega'' = 0)$, and figure 2(c) shows the forcing mode $\widehat{\boldsymbol{\phi}}_{n=3}(k_1 = 6, k_3 = 16, \omega = 0)$ forming the interaction. The streamwise components of the resolvent modes are shown with color bars, and the spanwise/wall-normal components are indicated with arrows. Note, the spanwise modes (i.e, K_3', k_3'', k_3) are provided for completeness, but their detailed analysis is outside the scope of the present work.

We next present results obtained from simulations of the ARNL model parametrized based on the two triadic relationships determined from the resolvent analysis: $(K_1', k_1'', k_1) = (2, 4, 6)$ and $(K_1', k_1'', k_1) = (2, 6, 8)$. The associated wavelengths Λ_1', λ_1'', and λ_1 are defined as $2\pi/K_1'$, $2\pi/k_1''$, and $2\pi/k_1$ respectively where capitalized symbols denote large scales. Table 1 summarizes the wave numbers and corresponding wavelengths used in the ARNL simulations. Here we also include the details of the half-channel RNL simulation [28], where the non-integer wavenumbers are due to a different streamwise domain used for normalization. Those simulations used three streamwise-varying modes, implying similar computational costs to the present ARNL simulations.

Table 1: Comparison of streamwise interactions in simulations

Case	Large scales $\mathcal{L}$	Small Scales $\mathcal{S}$		$\Lambda_1'^+$	$\lambda_1''^+$	λ_1^+
RNL [28]	0	$k_1' = 6, 6.5, 7$		-	188, 174, 162	-
ARNL-1	$0,\ K_1' = 2$	$k_1' = 4$	$k_1 = 6$	565	283	188
ARNL-2	$0,\ K_1' = 2$	$k_1' = 6$	$k_1 = 8$	565	188	141

Figure 3(a) shows the mean velocity profile obtained from both ARNL simulations alongside the RNL simulation data from [28], and DNS data [41], all at $Re_\tau = 180$. Here, and in what follows, the overbar indicates averaging in time and the horizontal directions. All cases overlap in the near-wall region, while the expected differences between the full and half channel configurations are seen in the wake region. While all of the cases show log law behavior, there are small differences in the slope and magnitude toward the center of the channel, with the DNS from [41] showing a higher velocity at the channel center than all of the other cases. The two ARNL cases show very minor differences in this region, indicating that the mean behavior is not significantly influenced by the choice of streamwise scale input. Figure 3(b-d) presents the streamwise, wall-normal, and spanwise normal Reynolds stresses, which enable further analysis of differences between simulations. In figure 3(b), all cases capture the wall-normal location of the $\overline{u_1u_1}^+$ peak, but only the ARNL-1 data accurately reproduces the magnitude throughout the channel. The RNL and ARNL-2 simulations over predict $\overline{u_1u_1}^+$. This over-prediction is consistent with prior RNL studies, where the restriction of the small scales to the peak region of the outer layer surrogate dissipation spectra, as well as the inclusion of additional small scales, improved the accuracy of these statistics [28, 33, 42]. Prior ARNL studies at higher Reynolds numbers with ad hoc selection of the large scales also led to over-predictions of this quantity [25]. The improvement here suggests that the inclusion of the additional nonlinear interactions in the ARNL versus RNL simulation, as well as the resolvent-informed parametrization of the ARNL model, leads to a more accurate representation of the dynamics. This improved accuracy is also seen in the other components, where continuity implies that an over-prediction of $\overline{u_1u_1}^+$ will result in an under-prediction of $\overline{u_2u_2}^+$ and $\overline{u_3u_3}^+$. In figure 3(c) and (d), both ARNL simulations better predict $\overline{u_2u_2}^+$ and $\overline{u_3u_3}^+$ when compared to the RNL. Specifically, ARNL-1 accurately captures the peak value of $\overline{u_3u_3}^+$ at its corresponding wall-normal location. The $\overline{u_3u_3}^+$ peaks at $x_2^+ \approx 35, 49, 33, 45$ for DNS, RNL, ARNL-1, and ARNL-2, respectively, indicating improved model accuracy near the wall where increased nonlinear interactions occur. These results suggest that incorporating resolvent-informed nonlinearity enhances the ARNL model's ability to capture near-wall turbulence dynamics.

Figure 4 shows the k_3 pre-multiplied spanwise energy spectra for the streamwise and wall-normal velocity fluctuations, respectively $k_3E_{u_1u_1}$ in panels (a)-(d) and $k_3E_{u_2u_2}$ in panels (e)-(h). Panels (a,e) show DNS [28] data, (b,f) RNL data [28], (c,g) ARNL-1 results, and (d,h) ARNL-2 results. The white dashed lines in each plot indicate the location of peak energy in the DNS. Figures 4(c) and (d) show that ARNL-1 and ARNL-2 simulations lead to improved predictions of the peak location of $k_3E_{u_1u_1}$ when compared to RNL simulations. A more detailed comparison between the DNS and RNL spectra can be found in [28]. The ARNL simulations lead to very similar quantitative features (shape, distribution over the wall normal direction) of the spectra to the DNS, despite the reduced streamwise wave number support of the ARNL models. The full shape of the spectra cannot be compared due to the smaller channel simulated, although the contours do appear to be closing at the outer edge of the domain, suggesting that the ARNL simulations may eliminate unphysical spread in the RNL spectra seen at longer wavelengths. Figure 4(g,h) also shows that the ARNL predicted $k_3E_{u_2u_2}$ is also more consistent with DNS data than the RNL. Both ARNL cases capture the energy distribution farther from the wall, as well as the location and shape of the peak region.

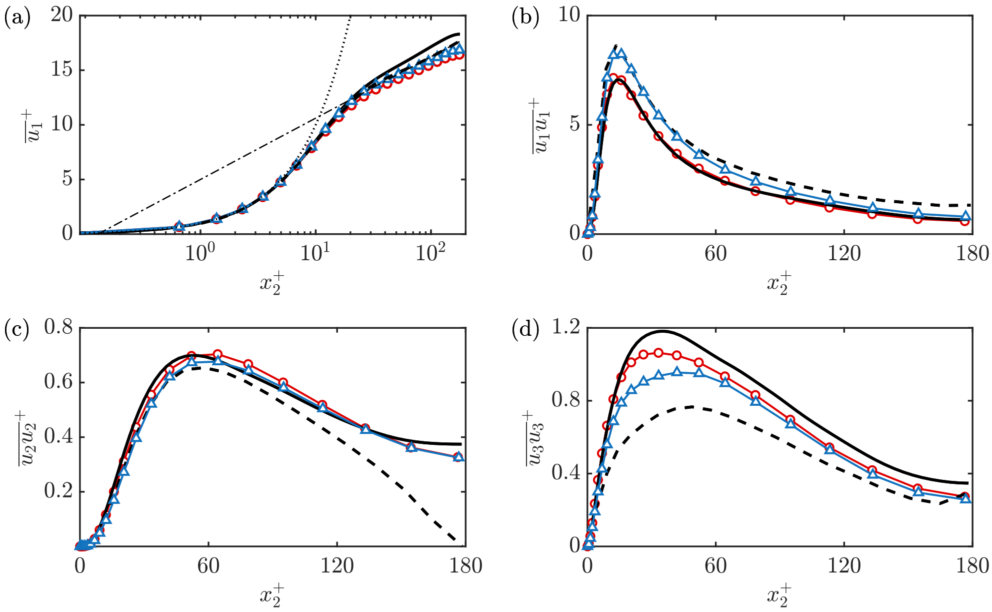

Figure 3: (a) Mean streamwise velocity profiles, and (b) streamwise, (c) wall-normal, and (d) spanwise Reynolds stresses for DNS [41] (black solid line, ——), RNL [28] (black dashed line, - - -), ARNL-1 $(K_1', k_1'', k_1) = (2, 4, 6)$ (red circles, –○–), and ARNL-2 $(K_1', k_1'', k_1) = (2, 6, 8)$ (blue triangles, –△–) at $Re_\tau = 180$. Dash-dotted line indicates $u_1^+ = 1/0.41\ ln(x_2^+) + 5$ and dotted line indicates $u_1^+ = x_2^+$.

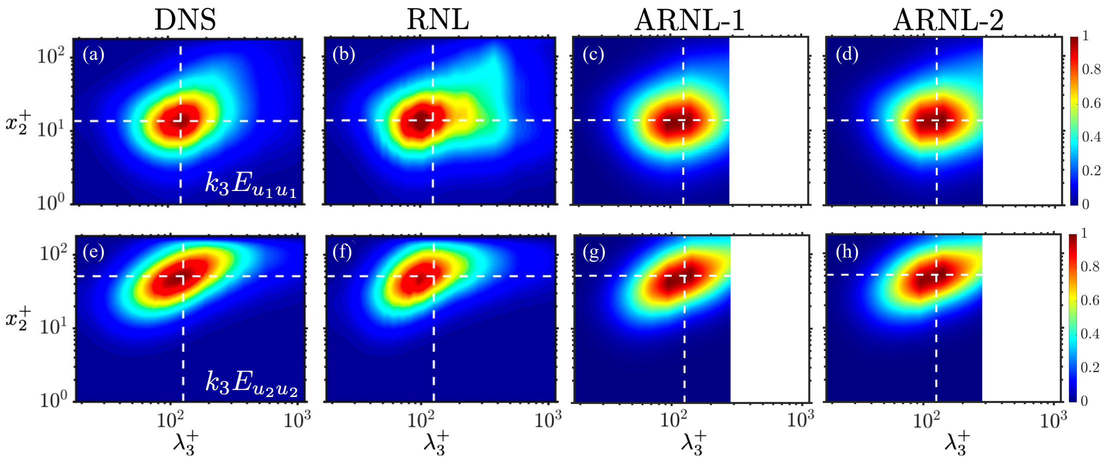

Figure 4: Pre-multiplied energy spectra, (a-d) $k_3 E_{u_1 u_1}$ and (e-h) $k_3 E_{u_2 u_2}$ normalized by global maximum comparing (a,e) DNS [28], (b,f) RNL [28], (c,g) ARNL-1, and (d,h) ARNL-2 simulations at $Re_\tau = 180$. White dashed lines indicate wall-normal distance and spanwise wavelength where the spectra from DNS peaks respectively, (a-d) $x_2^+ \approx 14$, $\lambda_3^+ \approx 126$ and (e-h) $x_2^+ \approx 51$, $\lambda_3^+ \approx 126$.

To gain deeper insight into the performance of the ARNL models, we compute the energy transport

$$0 = \underbrace{\overline{-\widetilde{u_1}\widetilde{u_2}}\frac{d\overline{u_T}}{dx_2}}_{\text{production}} - \underbrace{\overline{\nu(\nabla\widetilde{\boldsymbol{u}}):(\nabla\widetilde{\boldsymbol{u}})}}_{\text{pseudo-dissipation}} + \underbrace{\nu\frac{d^2\mathrm{k}}{dx_2^2}}_{\text{viscous transport}} - \underbrace{\frac{d}{dx_2}\overline{\frac{1}{2}\widetilde{u}_2\widetilde{\boldsymbol{u}}\cdot\widetilde{\boldsymbol{u}}}}_{\text{turbulent transport}} - \underbrace{\frac{1}{\rho}\frac{d}{dx_2}\overline{\widetilde{u}_2\widetilde{p}}}_{\text{pressure transport}} \tag{12}$$

given by [3]. Figure 5 presents the corresponding rates of the turbulent kinetic energy ($\mathrm{k} = \frac{1}{2}\overline{\widetilde{\boldsymbol{u}}\cdot\widetilde{\boldsymbol{u}}}$): production P_k, pseudo-dissipation $\widetilde{\epsilon}_\mathrm{k}$, viscous transport D_k, turbulent transport T_k, and pressure transport Π_k [3,42] in the near wall region $x_2^+ < 30$. The analysis focused on the near-wall region, as that was where the most pronounced discrepancies between the models were observed. Here, the production rates predicted by the ARNL and RNL models closely follow the DNS results, whereas the pseudo-dissipation rate and the total transport predicted by the ARNL models demonstrate improved agreement with the DNS data than the RNL case. The ARNL-1 simulation provides the best prediction of both the wall-normal location of the peaks and the corresponding magnitude across all quantities. Figure 5(d,e,f) (bottom panels) shows the individual transport terms. In the ARNL and RNL simulations, the viscous/diffusive (D_k) and pressure transport Π_k terms are over-predicted near the wall, while the turbulent transport T_k term is under-predicted in this same region. However, the ARNL-1 simulation provides considerable improvement in the accuracy relative to both RNL and ARNL-2, particularly in the prediction of both the value and wall normal locations of the peak values. The enhanced agreement in the total transport for ARNL-1 primarily arises from the improved representation of the diffusive and turbulent transport rates. The pressure transport contribution, by contrast, shows limited improvement and therefore plays a minor role in the overall enhancement of total transport. The pseudo-dissipation rate, viscous transport, and turbulent transport are accurately predicted at $x_2^+ \approx 15$, improving the balance among all terms. This suggests that, in the ARNL-1 case, no individual term needs to overcompensate for modeling discrepancies, resulting in a more physically consistent energy budget. This improvement may account for the better prediction of the Reynolds stresses seen in Figure 3.

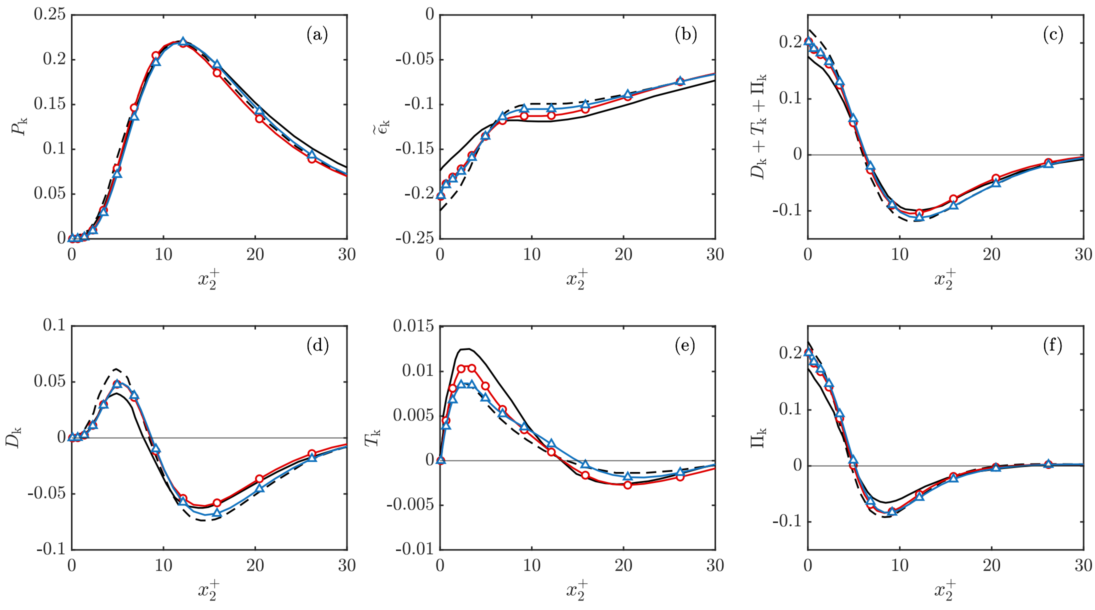

Figure 5: Terms of the turbulent kinetic energy budget for (a) production, (b) pseudo-dissipation, (c) total transport, (d) viscous transport, (e) turbulent transport, and (f) pressure transport for DNS [42] (black solid line, ——), RNL [42] (black dashed line, - - -), ARNL-1 $(K_1', k_1'', k_1) = (2, 4, 6)$ (red circles, —o—), and ARNL-2 $(K_1', k_1'', k_1) = (2, 6, 8)$ (blue triangles, —△—) at $Re_\tau = 180$.

The results above demonstrate that both of the resolvent-informed ARNL simulations provide improved model fidelity over RNL simulations, particularly in the higher-order statistics and spectra that are more sensitive to nonlinear scale interactions. The previously identified optimal streamwise wavelength support of the RNL perturbation dynamics at $Re_\tau = 180$ was $\lambda_1^+ = 162$ [33]. Later in [28,42], the optimal streamwise wave number support of the perturbation dynamics was shown to be associated with the peak region of the outer layer pseudo dissipation spectra, indicating that there is a range of values leading to improved model performance. The good performance of the ARNL-1 and ARNL-2 simulations is likely due to the correspondence of the small scales with this optimal region (see table 1). We note that $\lambda_1^+ = 565$ and $\lambda_1^+ = 283$ associated with the small scales in the $(K_1', k_1'', k_1) = (2, 2, 4)$ triad are both outside of the optimal range and significantly differ from the optimal streamwise wavelength of $\lambda_1^+ = 162$, which is why we chose not to analyze this case despite it having a larger value of α/α_{max}. In comparing the performance of the two ARNL simulations, the ARNL-1 simulation produced the most accurate results, which we attribute to the fact that the triad defining the nonlinear interactions contributing to the large scales has a higher α/α_{max} value than the ARNL-2 case. This behavior suggests that both the nonlinear interaction coefficient α/α_{max} and the range of small scales supporting the dynamics need to be considered when parameterizing the model. Further analysis over a wider range of Reynolds numbers and comprising additional nonlinear interaction pairs is needed to fully characterize an optimal procedure to define the streamwise wave number support within the ARNL model.

5 Conclusions and Future Work

In this study, we introduced a resolvent-based framework that requires only a turbulent mean velocity profile to estimate energetically relevant triadic interactions in channel flow. Unlike prior approaches that relied on DNS data to compute a nonlinear interaction coefficient, the proposed method relies on response modes obtained from the resolvent operator to estimate the nonlinear interactions (forcing) in the NSE. We first showed that this method provides similar predictions for the flow scales contributing to the largest energy transfer. We then focused on the streamwise wave number triads and used the results to inform the selection of streamwise scales in ARNL models, which achieve order reduction by limiting both the nonlinear interactions between streamwise varying modes and limiting the number of streamwise scales supporting the dynamics.

ARNL simulations at $Re_\tau = 180$ with the resolvent analysis informed parametrization demonstrated improved second-order statistics when compared to RNL simulations, which do not include nonlinear interactions between non-zero streamwise scales. In particular, the ARNL pre-multiplied spanwise energy spectra showed closer agreement with DNS data in terms of the overall shape of the spectra, the peak location, and the shape of the peak region. ARNL simulations also showed good agreement with DNS predictions of the pseudo-dissipation rate, viscous transport, and turbulent transport predictions in the near wall region. The ARNL simulation with the best performance had the second highest resolvent based nonlinear interaction coefficient but retained the small scales in the peak region of the outer layer peak dissipation spectra previously shown to lead to optimal RNL performance. These results demonstrated that obtaining nonlinear interaction coefficients using resolvent forcing modes provided a systematic means of identifying the correct streamwise interactions to include in an ARNL model. Future work involves employing the resolvent-based analysis approach introduced here to parametrize to higher Reynolds numbers ARNL simulations, which is where the additional nonlinear scale interactions are expected to make a larger difference in model performance, see e.g., [25].

Extending the resolvent analysis framework to include non-zero temporal frequencies (i.e., $\omega \neq 0$) is another direction for future work that may enable analysis of the dynamic behavior of the nonlinear interactions. Finally, broadband forcing was assumed in all calculations of the nonlinearity, so extending to colored noise by extracting nonlinear interaction weights via DNS data or iteratively computing from ARNL simulations could improve the modeling of the nonlinear term.

6 Acknowledgments

This work was supported in part by the European Research Council under the Caust grant ERC-AdG-101018287. Computations were performed at the Advanced Research Computing at Hopkins (ARCH) core facility (rockfish.jhu.edu), supported by the National Science Foundation (NSF) grant number OAC1920103. A. Risha acknowledges support from the Department of Defense (DoD) through the National Defense Science and Engineering Graduate (NDSEG) fellowship program. E. Lenz acknowledges support from the NSF Graduate Research Fellowship under grant number DGE-1745301. B. Viggiano acknowledges support from NSERC through the grant number RGPIN-2025-07209. H. J. Bae acknowledges support from the Air Force Office of Scientific Research under grant number FA9550-22-1-0109. All authors acknowledge Prof. Scott Dawson for reviewing an early version of the manuscript and Prof. Javier Jiménez for organizing the 2025 Madrid Turbulence Summer Workshop.

References

[1] Hamilton K, Kim J and Waleffe F 1995 J. Fluid Mech. **287** 317–348

[2] Jiménez J and Pinelli A 1999 J. Fluid Mech. **389** 335–359

[3] Pope S B 2000 Turbulent Flows (Cambridge, UK: Cambridge University Press) ISBN 978-0-521-59125-6

[4] Cossu C and Hwang Y 2016 Phil. Trans. R. Soc. A **375** 20160088

[5] Jovanović M R and Bamieh B 2005 J. Fluid Mech. **534** 145–183

[6] McKeon B J and Sharma A S 2010 J. Fluid Mech. **658** 336–382

[7] Sharma A S and McKeon B J 2013 J. Fluid Mech. **728** 196–238

[8] McKeon B J, Sharma A and Jacobi I 2013 Phys. Fluids **25** 031301

[9] Symon S, Rosenberg K, Dawson S T M and McKeon B J 2018 Phys. Rev. Fluids **3** 053902

[10] Farrell B F and Ioannou P J 2024 Phys. Rev. Fluids **9** 024605

[11] Rolandi L V, Ribeiro J H M, Yeh C A and Taira K 2024 Theor. Comput. Fluid Dyn. **38** 603–639

[12] Moarref R, Jovanović M R, Tropp J A, Sharma A S and McKeon B J 2014 Phys. Fluids **26** 051701

[13] Zare A, Jovanović M R and Georgiou T T 2017 J. Fluid Mech. **812** 636–680

[14] Beneddine S, Sipp D, Arnault A, Dandois J and Lesshafft L 2016 J. Fluid Mech. **798** 485–504

[15] Rosenberg K, Symon S and McKeon B J 2019 Phys. Rev. Fluids **4** 052601

[16] Morra P, Nogueira P A S, Cavalieri A V G and Henningson D S 2021 J. Fluid Mech. **907** A24

[17] Bae H J, Lozano-Durán A and McKeon B J 2021 J. Fluid Mech. **914** A3

[18] Symon S, Illingworth S J and Marusic I 2021 J. Fluid Mech. **911** A3

[19] Karban U, Martini E, Cavalieri A V G and Jordan P 2023 arXiv preprint arXiv:2301.01078

[20] Huang Y, Toedtli S S, Chini G P and McKeon B J 2023 arXiv preprint arXiv:2305.00095

[21] Yeung B, Chu T and Schmidt O T 2024 arXiv preprint arXiv:2411.12057

[22] Ballouz E, Dawson S T M and Bae H J 2025 J. Fluid Mech. **1016** A19

[23] Cho M, Hwang Y and Choi H 2018 J. Fluid Mech. **854** 474–504

[24] Ding J, Chung D and Illingworth S J 2025 J. Fluid Mech. **1002** A42

[25] Minnick B A, Viggiano B and Gayme D F 2023 Augmented restricted nonlinear (ARNL) model for high Reynolds number wall-turbulence Conf. on Interdisciplinary Turbulence Initiative pp 65–75

[26] Thomas V, Lieu B K, Jovanović M R, Farrell B F, Ioannou P and Gayme D F 2014 Phys. Fluids **26** 105112

[27] Farrell B F, Gayme D F and Ioannou P J 2017 Phil. Trans. R. Soc. A **375** 20160081

[28] Gayme D F and Minnick B A 2019 Phys. Rev. Fluids **4** 110505

[29] Kim K J and Adrian R J 1999 Phys. Fluids **11** 417–422

[30] Hutchins N and Marusic I 2007 J. Fluid Mech. **579** 1–28

[31] Smits A J, McKeon B J and Marusic I 2011 Annu. Rev. Fluid Mech. **43** 353–375

[32] Farrell B F, Ioannou P J, Jiménez J, Constantinou N C, Lozano-Durán A and Nikolaidis M A 2016 J. Fluid Mech. **809** 290–315

Journal of Physics: Conference Series **3230** (2026) 012002 doi:10.1088/1742-6596/3230/1/012002

[33] Bretheim J U, Meneveau C and Gayme D F 2015 Phys. Fluids **27** 011702

[34] Marston J B, Chini G P and Tobias S M 2016 Phys. Rev. Lett. **116** 214501

[35] Tobias S M and Marston J B 2017 J. Fluid Mech. **810** 412–428

[36] Hernández C G, Yang Q and Hwang Y 2022 J. Fluid Mech. **936** A33

[37] Viggiano B, Camobreco C, Wong J, Luhar M, García-Mayoral R, Chung D and Gayme D F 2024 The role of nonlinear interactions in the onset of drag increase in flow over riblets J. Phys: Conf. Series vol 2753 p 012010

[38] McKeon B J 2019 EPSRC Summer School on Modal Decompositions in Fluid Mechanics

[39] Thomas V L, Farrell B F, Ioannou P J and Gayme D F 2015 Phys. Fluids **27** 105104

[40] Vinokur M 1983 J. Comp. Phys. **50** 215–234 ISSN 00219991

[41] Moser R D, Kim J and Mansour N N 1999 Phys. Fluids **11** 943–945

[42] Minnick B A and Gayme D F 2019 Characterizing energy transfer in restricted nonlinear wall-bounded turbulence Int Sym Turbulence and Shear Flow Phenomena (TSFP-11)